Numerical Simulation of Free Surface Affected by Submarine with a Rotating Screw Moving Underwater

Masashi Yamakawa[1], Kohei Yoshioka[1], Shinichi Asao[2], Seiichi Takeuchi[2], Atsuhide Kitagawa[1], and Kyohei Tajiri[1]

[1] Kyoto Institute of Technology, Matsugasaki Sakyo-ku Kyoto 606-8585, Japan
[2] College of Industrial Technology, Nishikoya, Amagasaki, Hyogo 661-0047, Japan
yamakawa@kit.ac.jp

Abstract. We conducted a numerical simulation of the free surface affected by the diving movement of an object such as a submarine. We have already proposed a computation method that combines the moving grid finite volume method and a surface height function method. In this case, the dive movement was expressed only as a traveling motion, not as a deformation. To express the deformation of a body underwater, the unstructured moving grid finite volume method and sliding mesh approach are combined. The calculation method is expected to be suitable for a computation with high versatility. After the scheme was validated, it was put to practical use. The free surface affected by a submarine with a rotating screw moving underwater was computed using the proposed method. Owing to the computation being for a relatively shallow depth, a remarkable deformation of the free surface occurred. In addition, the movement of the submarine body had a more dominant effect than a screw rotation on changing the shape of the free water surface.

Keywords: Free surface, Moving grid, Submarine.

1 Introduction

Studying how the shape of the free water surface is affected by the movement of submerged bodies is very useful and interesting from not only an engineering perspective but also a computational science perspective. For example, such studies could be carried out in the preliminary design of the shape and placement of wave activated power generators [1]. In addition, it would be useful for designing underwater exploration submersibles [2]. Furthermore, a lot of basic research on interactions between the free surface and the motion of submerged objects have been reported [3]. Benusiglio et al. [4] investigated the drag and shape of waves caused by a moving small sphere under the water. But, as there are a lot of complicated flows with the free surface, from the perspectives on experimental equipment cost and flow reproducibility, the applied flow fields have had to be simple. In a previous study using numerical simulations, Kwag et al. [5] investigated the shape of the free surface when varying the distance between a three dimensional airfoil and the surface and when varying the attack angle of the airfoil to the surface. In addition, Moonesun et al. [6] compared computational results and

ICCS Camera Ready Version 2021
To cite this paper please use the final published version:
DOI: 10.1007/978-3-030-77980-1_21

experimental results of the interaction between the free water surface and a submersible in rectilinear motion. However, the reproducibility of the motion itself and of the resulting shapes upon modeling were limited.

In general, computational methods for the interface can be classified into two broad categories: interface tracking methods [7] and interface capturing methods. In the interface tracking method as represented by the Arbitrary Lagrangian-Eulerian method, an interface is expressed directly by moving and deforming a mesh according to the motion of the interface. On the other hand, in the interface capturing method represented by the Volume of Fluid method or the level set method, an interface is expressed indirectly using a function indicating the interface on a fixed mesh. The interface capturing method is suitable for expressing a separation or large deformation of the interface. Thus, it is often used to solve such interface problems. However, it is difficult to express the interface with a moving body, because it is not easy for the method to maintain the calculation accuracy for a flow around the moving body. For this reason, this study used the interface tracking method, in which it is relatively easy to maintain the calculation accuracy around an interface. The method is used together with the unstructured moving grid finite volume method [8, 9] and the moving computational domain method to avoid calculation failures. Furthermore, the combination of these methods permits removal of body movement restrictions and generation of flexible meshes. However, the method has not been applied to a flow around a body with a complicated motion such as an oscillatory heaving motion and rotational motion yet. Thus, in this paper, it was applied to a free surface affected by a submarine with a rotating screw moving underwater.

2 Numerical Approach

2.1 Governing equations

The governing equations are composed of the following three-dimensional (3D) continuity equation and Navier-Stokes equation for incompressible flows written in conservation law form.

$$\frac{\partial u}{\partial x} + \frac{\partial v}{\partial y} + \frac{\partial w}{\partial z} = 0 \tag{1}$$

$$\frac{\partial \mathbf{q}}{\partial t} + \frac{\partial \mathbf{E}}{\partial x} + \frac{\partial \mathbf{F}}{\partial y} + \frac{\partial \mathbf{G}}{\partial z} - \frac{1}{Re}\left(\frac{\partial \mathbf{E_v}}{\partial x} + \frac{\partial \mathbf{F_v}}{\partial y} + \frac{\partial \mathbf{G_v}}{\partial z}\right) = \mathbf{H_g} \tag{2}$$

where,

$$\mathbf{q} = \begin{pmatrix} u \\ v \\ w \end{pmatrix}, \ \mathbf{E} = \begin{pmatrix} u^2 + p \\ uv \\ uw \end{pmatrix}, \ \mathbf{F} = \begin{pmatrix} uv \\ v^2 + p \\ vw \end{pmatrix}, \ \mathbf{G} = \begin{pmatrix} uw \\ vw \\ w^2 + p \end{pmatrix}, \tag{3}$$

ICCS Camera Ready Version 2021
To cite this paper please use the final published version:
DOI: 10.1007/978-3-030-77980-1_21

$$\mathbf{E_v} = \begin{pmatrix} u_x \\ v_x \\ w_x \end{pmatrix},\ \mathbf{F_v} = \begin{pmatrix} u_y \\ v_y \\ w_y \end{pmatrix},\ \mathbf{G_v} = \begin{pmatrix} u_z \\ v_z \\ w_z \end{pmatrix},\ \mathbf{H}_{\boldsymbol{g}} = \begin{pmatrix} 0 \\ 0 \\ -\frac{1}{Fr^2} \end{pmatrix}.$$

Here, $\mathbf{q}$ is a conservative quantity, $\mathbf{E}$, $\mathbf{F}$ and $\mathbf{G}$ are inviscid flux vectors in the x, y, z directions, $\mathbf{E_v}$, $\mathbf{F_v}$ and $\mathbf{G_v}$ are viscous flux vectors, $\mathbf{H}_{\boldsymbol{g}}$ is a gravity flux vector, and u, v, w are velocity components in the x, y, z directions respectively. p is pressure, Re is Reynolds number, Fr is Froude number, while the x, y and z subscripts represent the differential in each direction.

2.2 Numerical scheme

The free surface and rotating object are expressed as a moving mesh using the moving grid finite volume method. The method estimates a control volume in the unified space-time domain. So, to express 3D movement, the method uses a four-dimensional (4D) domain to satisfy a geometric conservation law as well as a physical conservation law. As the discretization of the method, Eq. (2) is separated into a velocity vector term and a pressure vector term as shown in Eq. (4).

$$\hat{\mathbf{E}} = \mathbf{E} - \mathbf{P_1},\ \hat{\mathbf{F}} = \mathbf{F} - \mathbf{P_2},\ \hat{\mathbf{G}} = \mathbf{G} - \mathbf{P_3} \tag{4}$$

where,

$$\hat{\mathbf{E}} = \begin{pmatrix} u^2 \\ uv \\ uw \end{pmatrix}, \hat{\mathbf{F}} = \begin{pmatrix} uv \\ v^2 \\ vw \end{pmatrix}, \hat{\mathbf{G}} = \begin{pmatrix} uw \\ vw \\ w^2 \end{pmatrix}, \mathbf{P_1} = \begin{pmatrix} p \\ 0 \\ 0 \end{pmatrix}, \mathbf{P_2} = \begin{pmatrix} 0 \\ p \\ 0 \end{pmatrix}, \mathbf{P_3} = \begin{pmatrix} 0 \\ 0 \\ p \end{pmatrix}. \tag{5}$$

Eq. (2) can be rewritten as follows by using the above equations.

$$\frac{\partial \mathbf{q}}{\partial t} + \frac{\partial \hat{\mathbf{E}}}{\partial x} + \frac{\partial \hat{\mathbf{F}}}{\partial y} + \frac{\partial \hat{\mathbf{G}}}{\partial z} - \frac{1}{Re}\left(\frac{\partial \mathbf{E}_v}{\partial x} + \frac{\partial \mathbf{F}_v}{\partial y} + \frac{\partial \mathbf{G}_v}{\partial z}\right) + \frac{\partial \mathbf{P_1}}{\partial x} + \frac{\partial \mathbf{P_2}}{\partial y} + \frac{\partial \mathbf{P_3}}{\partial z} = \mathbf{H}_{\boldsymbol{g}} \tag{6}$$

The equation is separated into Eq. (7) and (8) in order to perform the fractional step method.

$$\frac{\partial \mathbf{q}}{\partial t} + \frac{\partial \hat{\mathbf{E}}}{\partial x} + \frac{\partial \hat{\mathbf{F}}}{\partial y} + \frac{\partial \hat{\mathbf{G}}}{\partial z} - \frac{1}{Re}\left(\frac{\partial \mathbf{E}_v}{\partial x} + \frac{\partial \mathbf{F}_v}{\partial y} + \frac{\partial \mathbf{G}_v}{\partial z}\right) = \mathbf{H}_{\boldsymbol{g}} \tag{7}$$

$$\frac{\partial \mathbf{q}}{\partial t} + \frac{\partial \mathbf{P_1}}{\partial x} + \frac{\partial \mathbf{P_2}}{\partial y} + \frac{\partial \mathbf{P_3}}{\partial z} = 0 \qquad (\because 0 = [0 \quad 0 \quad 0]^T) \tag{8}$$

Eq. (7) is integrated over the control volume in the unified space-time domain and can be written as

$$\int_\Omega \left[\frac{\partial \mathbf{q}}{\partial t} + \frac{\partial \hat{\mathbf{E}}}{\partial x} + \frac{\partial \hat{\mathbf{F}}}{\partial y} + \frac{\partial \hat{\mathbf{G}}}{\partial z} - \frac{1}{Re}\left(\frac{\partial \mathbf{E}_v}{\partial x} + \frac{\partial \mathbf{F}_v}{\partial y} + \frac{\partial \mathbf{G}_v}{\partial z}\right)\right] d\Omega = \int_\Omega \mathbf{H}_{\boldsymbol{g}} d\Omega \tag{9}$$

ICCS Camera Ready Version 2021
To cite this paper please use the final published version:
DOI: 10.1007/978-3-030-77980-1_21

The equation is rewritten in terms of a divergence integral over a volume V_Ω in the 4D domain.

$$\int_\Omega \left[\left(\frac{\partial}{\partial x},\frac{\partial}{\partial y},\frac{\partial}{\partial z},\frac{\partial}{\partial t}\right)\left\{\left(\hat{\mathbf{E}}-\frac{1}{Re}\mathbf{E}_v\right),\left(\hat{\mathbf{F}}-\frac{1}{Re}\mathbf{F}_v\right),\left(\hat{\mathbf{G}}-\frac{1}{Re}\mathbf{G}_v\right),\mathbf{q}\right\}\right] d\Omega = V_\Omega \mathbf{H}_{\boldsymbol{g}} \quad (10)$$

Using Gauss' theorem, the equation can be written as

$$\oint_\Omega \left[\left\{\left(\hat{\mathbf{E}}-\frac{1}{Re}\mathbf{E}_v\right),\left(\hat{\mathbf{F}}-\frac{1}{Re}\mathbf{F}_v\right),\left(\hat{\mathbf{G}}-\frac{1}{Re}\mathbf{G}_v\right),\mathbf{q}\right\}(n_x,n_y,n_z,n_t)\right] dS = V_\Omega \mathbf{H}_{\boldsymbol{g}} \quad (11)$$

$$\sum_{l=1}^{6}\left[\mathbf{q}n_t+\left(\hat{\mathbf{E}}-\frac{1}{Re}\mathbf{E}_v\right)n_x+\left(\hat{\mathbf{F}}-\frac{1}{Re}\mathbf{F}_v\right)n_y+\left(\hat{\mathbf{G}}-\frac{1}{Re}\mathbf{G}_v\right)n_z\right]_l = V_\Omega \mathbf{H}_{\boldsymbol{g}} \quad (12)$$

Finally, the discretization for the governing equation is as follows.

$$\mathbf{q}^{n+1}(n_t)_6+\mathbf{q}^{n}(n_t)_5+\sum_{l=1}^{4}\left[\mathbf{q}^{n+1/2}n_t+\boldsymbol{\Phi}^{n+1/2}-\boldsymbol{\Psi}^{n+1/2}\right]_l = V_\Omega \mathbf{H}_{\boldsymbol{g}} \quad (13)$$

where, $n_x, n_y, n_z,$ and n_t are normal unit vectors in the *x*, *y*, *z* and *t* directions, respectively, and $\boldsymbol{\Phi}$ and $\boldsymbol{\Psi}$ are as follows.

$$\boldsymbol{\Phi} = \hat{\mathbf{E}}n_x+\hat{\mathbf{F}}n_y+\hat{\mathbf{G}}n_z \quad (14)$$

$$\boldsymbol{\Psi} = \frac{1}{Re}\left(\mathbf{E}_v n_x+\mathbf{F}_v n_y+\mathbf{G}_v n_z\right) \quad (15)$$

The pressure equation (8) is discretized as

$$(\mathbf{q}^{n+1}-\mathbf{q}^{*})(n_t)_6+\sum_{l=1}^{4}\left(\tilde{\mathbf{P}}_{\mathbf{1}}n_x+\tilde{\mathbf{P}}_{\mathbf{2}}n_y+\tilde{\mathbf{P}}_{\mathbf{3}}n_z\right)_l = 0 \quad (16)$$

Equations (13) and (16) are iteratively solved using the lower-upper symmetric-Gauss-Seidel (LU-SGS) method [10] and using the bi-conjugate gradient stabilized (Bi-CGSTAB) method [11], respectively. Here, the convective flux vectors are evaluated with the second-order upwind difference scheme. The viscous-flux and pressure vectors are evaluated with the central difference scheme.

3 Application to Submarine with Rotating Screw

3.1 Sliding mesh approach

A sliding mesh approach [12] was used to express the rotating screw in the simulation around a submarine. Here, the embedded sub computational domain rotates in the main domain. So far, we have used this approach only for compressible flows. Here, we devise an efficient approach for an incompressible flow.

ICCS Camera Ready Version 2021
To cite this paper please use the final published version:
DOI: 10.1007/978-3-030-77980-1_21

The sliding approach, which divides up the computational domain and slides its boundary, is a moving grid method. The physical values between domains are interpolated through the boundary surface. The sliding surface is dealt with as a moving boundary. To satisfy the geometric conservation law on the moving boundary, a conservative quantity $\mathbf{q}_{\text{ghost } i}$ is obtained as a boundary condition. A schematic diagram of the sliding surface is shown in Figure 1, and Eq. (17) defines $\mathbf{q}_{\text{ghost } i}$ using the overlapping area S_{ij}.

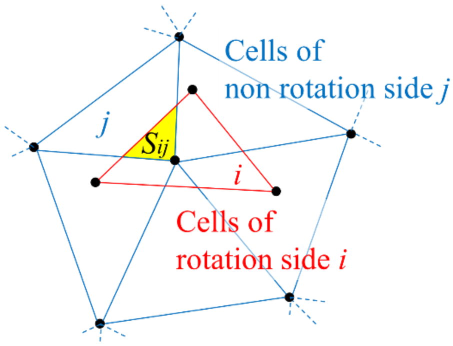

Fig. 1 Schematic diagram of sliding surface.

$$\mathbf{q}_{\text{ghost } i} = \frac{\sum_{j \in i} \mathbf{q}_j S_{ij}}{\sum_{j \in i} S_{ij}} \tag{17}$$

3.2 Verification of sliding mesh approach

A uniform flow on a sliding mesh was computed to verify the sliding mesh approach for an incompressible environment. Figure 2 shows the rotating embedded domain (Domain 2) set in the main domain (Domain 1), while Figure 3 shows the computational mesh, including the embedded rotating mesh in the main mesh and a horizontal cross section.

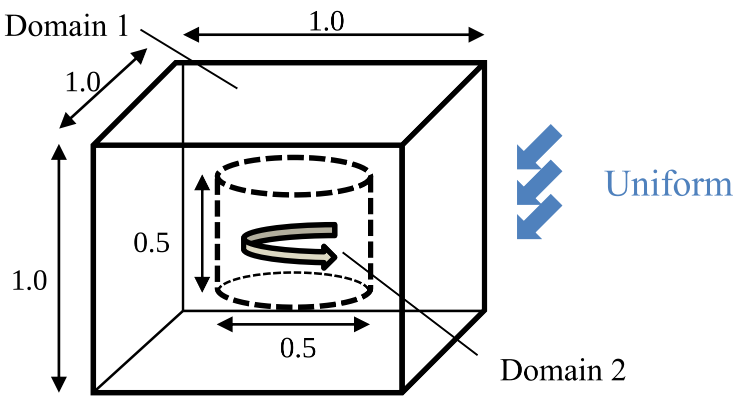

Fig. 2 Computational domain.

ICCS Camera Ready Version 2021
To cite this paper please use the final published version:
DOI: 10.1007/978-3-030-77980-1_21

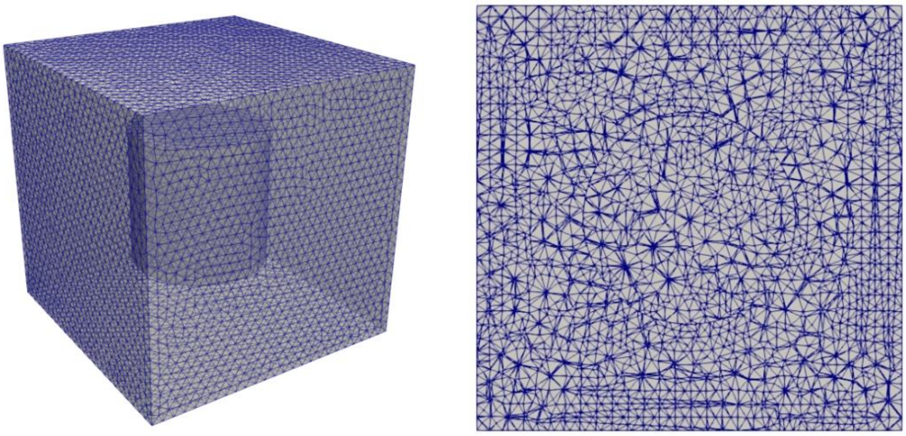

Fig. 3 Computational mesh (Left: whole mesh, Right: horizontal cross section).

The mesh was generated using MEGG3D [13]. The total number of elements was 153,301. A uniform flow ($u = v = w = 1.0$) was set as the initial condition. The velocities on all boundaries were fixed to be a uniform flow ($u = v = w = 0$). Regarding the other computational conditions, the angular velocity of the embedded domain was set to 1.0, and the Reynolds number was set to 100.

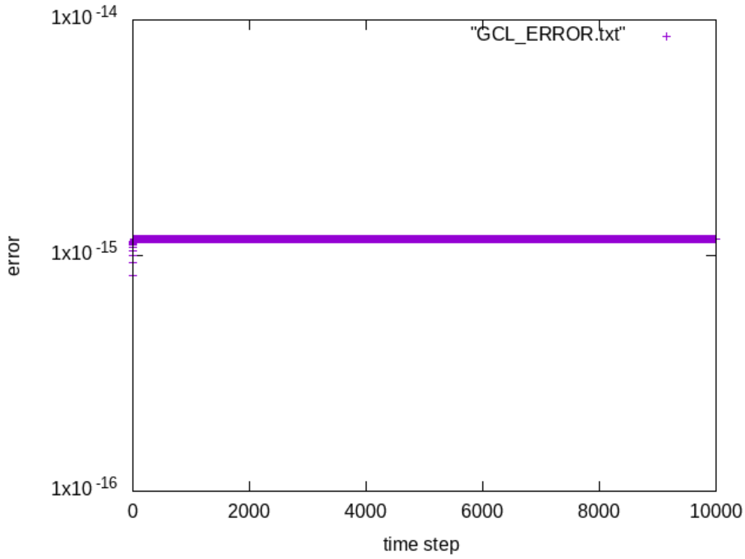

Fig. 4 History of velocity error.

ICCS Camera Ready Version 2021
To cite this paper please use the final published version:
DOI: 10.1007/978-3-030-77980-1_21

Figure 4 shows the history of the velocity error in the rotating embedded mesh system. The error is defined in Eq. (18). Here, $imax$ is the number of cell in the computational domain. The order of the error is 10^{-15}, which indicates machine zero. Thus, the geometric conservation law is satisfied between the rotating embedded mesh and fixed main mesh.

$$Error = \left\{\left(\sum_{i=1}^{imax}(u_i - 1.0)^2 + \sum_{i=1}^{imax}(v_i - 1.0)^2 + \sum_{i=1}^{imax}(w_i - 1.0)^2\right)/(3 \times imax)\right\}^{\frac{1}{2}} \quad (18)$$

3.3 Submarine model

A submarine with a rotating screw was chosen as a complicated shape and motion for study. A simplified model of the computation is shown in Figure 5.

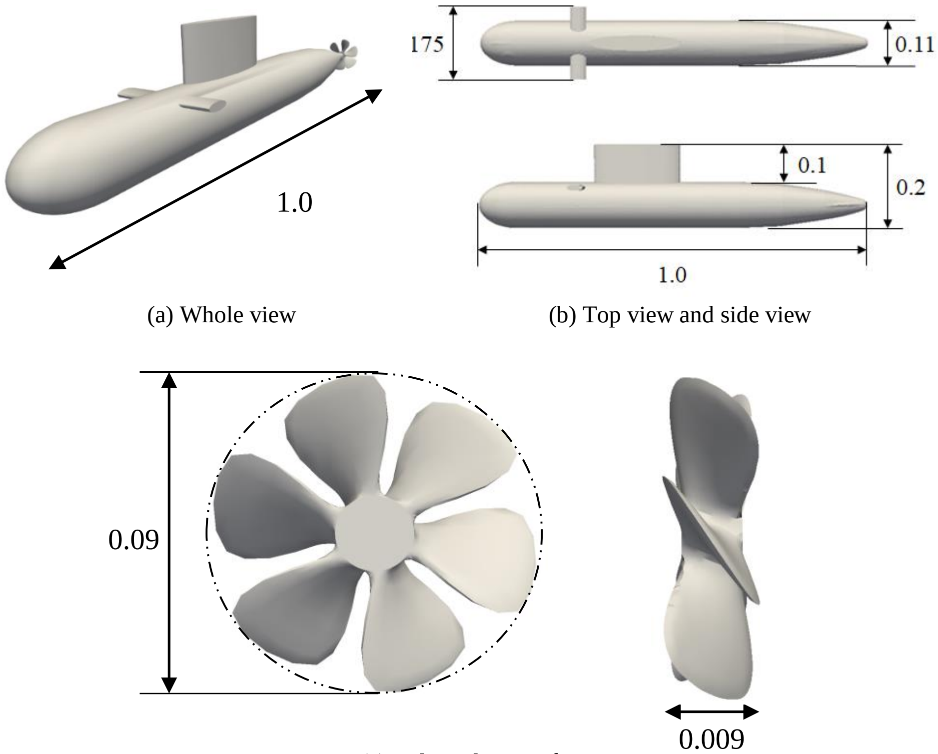

(c) Enlarged view of screw

Fig. 5 Submarine model.

Figure 6 shows the computational domain. The shape of the domain is like that of a bean cut in half along its broadest length. The top plane is the free water surface. The shape of the computational domain changes according to the motion of the free surface caused by the movement of the submarine. The shapes of the boundaries other than the top plane are fixed. The submarine is placed at a depth of 1.0, as shown in Figure 6.

ICCS Camera Ready Version 2021
To cite this paper please use the final published version:
DOI: 10.1007/978-3-030-77980-1_21

Cross-sections of mesh around the submarine and the whole computational domain are shown in Figure 7. The figure illustrates the fine mesh around the submarine and the screw.

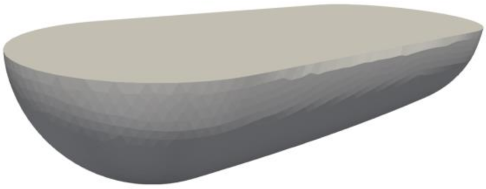

(a) Shape of computational domain

(b) Side view and front view of computational domain

Fig. 6 Computational domain.

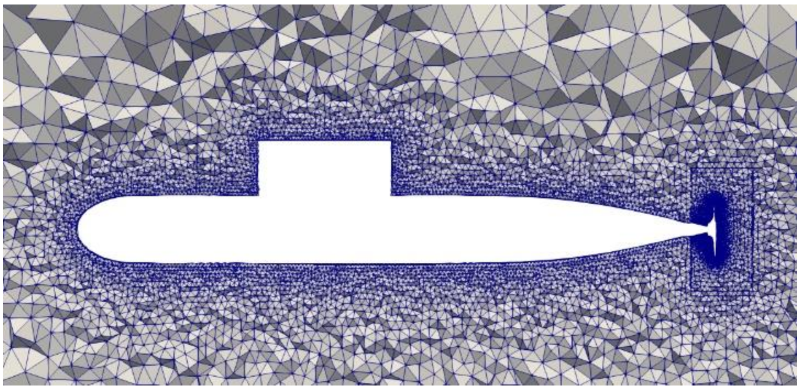

(a) Cross section of mesh around submarine

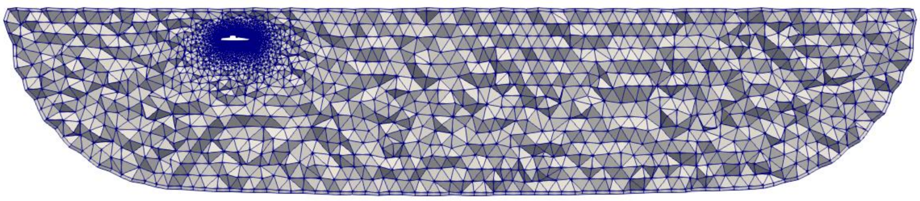

(b) Cross-section of mesh of whole domain

Fig. 7 Cross-section of mesh of submarine and whole domain.

The meshes around the screw are shown in Figure 8. A cylindrical mesh around the screw is embedded in the whole mesh, and it is placed at the rear of the submarine. The cylindrical mesh can be rotated using the sliding mesh approach in accordance with the rotation of the screw.

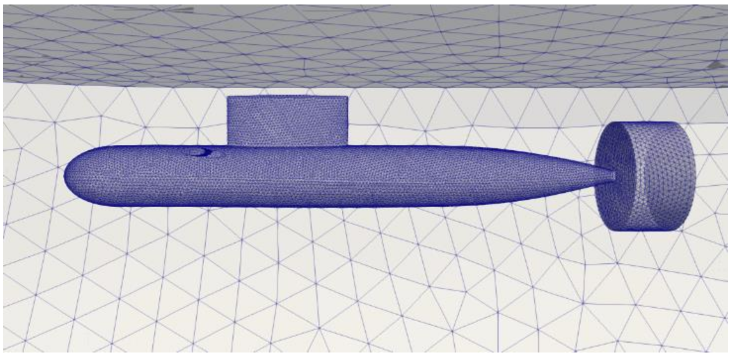

(a) Submarine surface mesh and embedded mesh around the screw

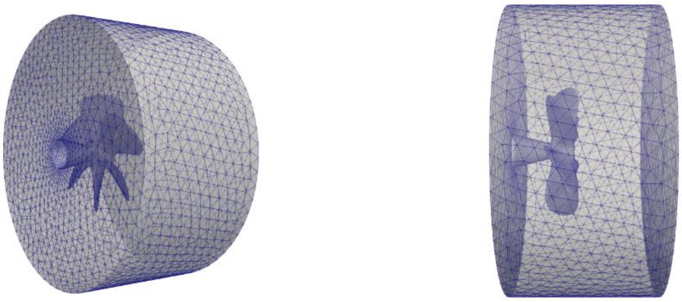

(b) Embedded computational domain and mesh around the screw

Fig. 8 Embedded mesh around the screw and placement for the submarine.

3.4 Computation for translator movement

The flow around the submarine for translator movement with a rotating screw was computed. The motion of the submarine was in a straight line keeping an initial depth of 1.0, as shown in Figure 9. The computational conditions are listed in Table 1.

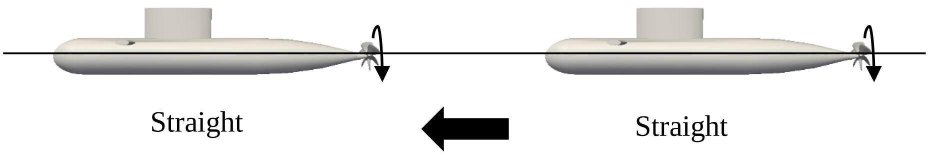

Fig. 9 Schematic diagram of translator movement.

ICCS Camera Ready Version 2021
To cite this paper please use the final published version:
DOI: 10.1007/978-3-030-77980-1_21

Table 1. Computational conditions for translator movement.

Total number of elements		1,158,625
Reynolds number Re		100
Froude number Fr		2.0
Time step Δt		0.001
Acceleration a		0.2 ($t \leq 5.0$) 0 ($t > 5.0$)
Initial conditions		Velocity: $u = v = w = 0.0$ Pressure: Determined from height
Boundary condition	Free surface	Velocity: Extrapolation Pressure: $p = 0.0$
	Forward	Velocity: $u = v = w = 0.0$ Pressure: Determined from height
	Submarine (with screw)	Velocity: Non-slip Pressure: Neumann
	Sliding surface	Sliding boundary condition
	Others	Velocity: Extrapolation Pressure: Determined from height

Figures 10 and 11 show velocity contours in the *x*-dirction and *z*-direction in side-view cross section. The ups and downs of the free water surface increase as time proceeds. In Figure 11, a negative velocity appears behind the submarine as an effect of the rotating screw. The heights of the free surfaces are shown in Figure 12. The height of the surface behind the submarine recovers after a drop.

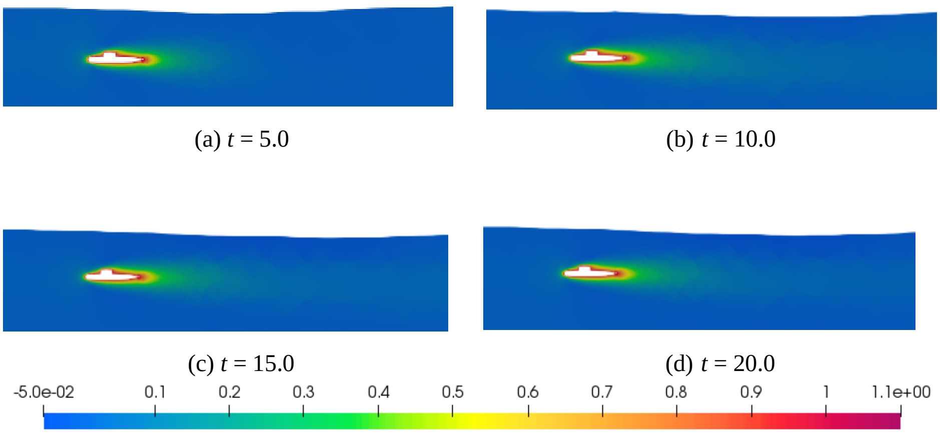

(a) t = 5.0 (b) t = 10.0

(c) t = 15.0 (d) t = 20.0

Fig. 10 *x*-direction velocity contours.

ICCS Camera Ready Version 2021
To cite this paper please use the final published version:
DOI: 10.1007/978-3-030-77980-1_21

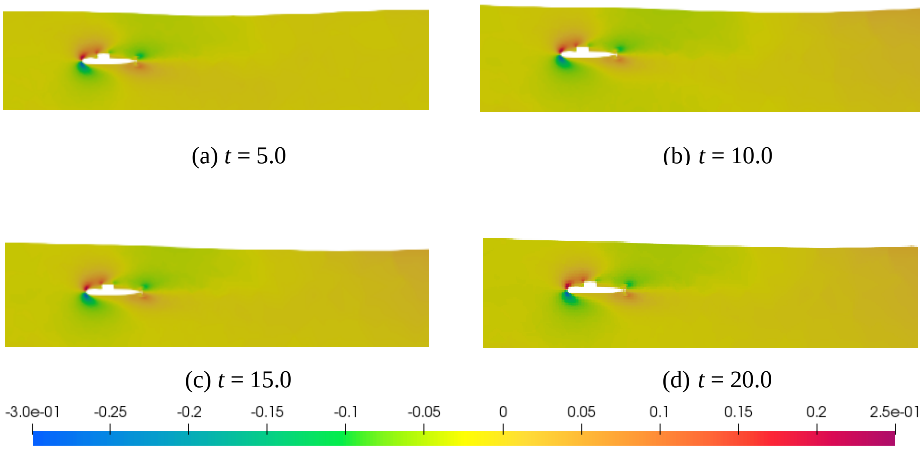

Fig. 11 z-direction velocity contours.

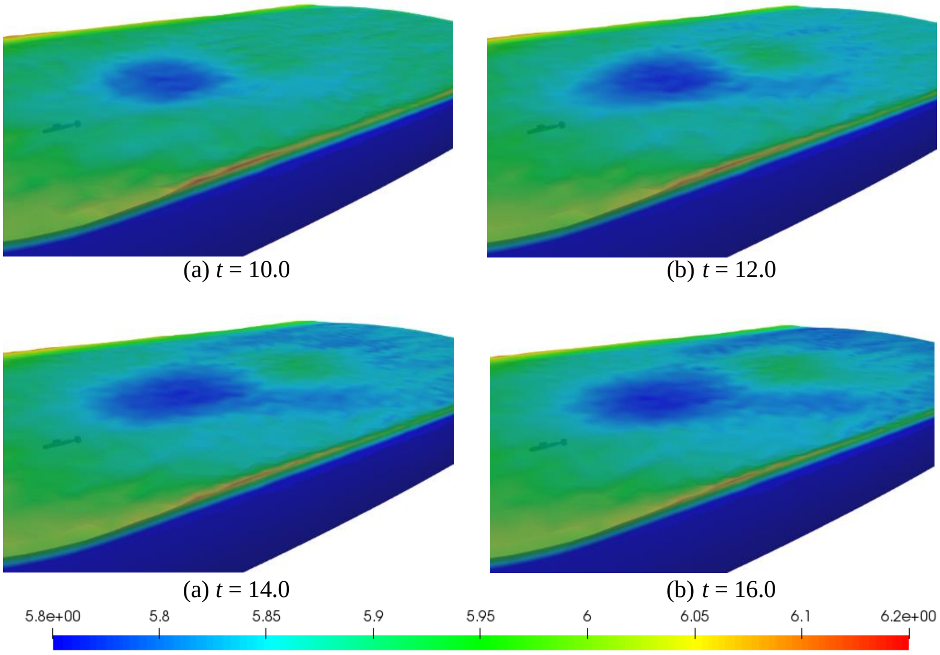

Fig. 12 Height of free surface.

ICCS Camera Ready Version 2021
To cite this paper please use the final published version:
DOI: 10.1007/978-3-030-77980-1_21

3.5 Computation for translator movement with rising motion

In addition to the translator movement, the rising motion of the submarine was simulated. A schematic diagram of the motion is shown in Figure 13. The calculation conditions are listed in Table 2.

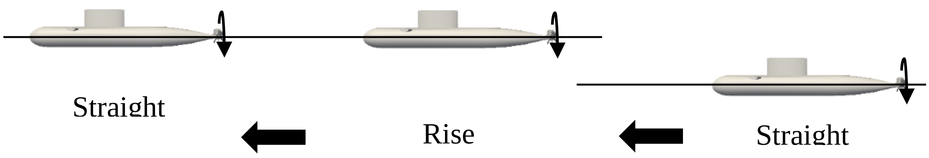

Fig. 13 Schematic diagram of translator movement with rising motion.

Table 2. Computational conditions for translator movement with rising motion.

Total number of elements		1,158,625
Reynolds number Re		100
Froude number Fr		2.0
Time step Δt		0.001
Acceleration a		$0.2\ (t \leq 5.0)$ $0\ (t > 5.0)$
Initial conditions		Velocity: $u = v = w = 0.0$ Pressure: Determined from height
Submarine rise		$z = \mathrm{A}\sin\left(\omega t - \frac{\pi}{2}\right)\ (\mathrm{A} = 0.2, \omega = \frac{\pi}{3.75})$ $(5.0 < t \leq 9.0)$
Boundary condition	Free surface	Velocity: Extrapolation Pressure: $p = 0.0$
	Forward	Velocity: $u = v = w = 0.0$ Pressure: Determined from height
	Submarine (with screw)	Velocity: Non-slip Pressure: Neumann
	Sliding surface	Sliding boundary condition
	Others	Velocity: Extrapolation Pressure: Determined from height

Figures 14 and 15 respectively show the velocity contours in the *x*-direction and *z*-direction in the case of a rising submarine. The velocity contours are similar to the previous case. However, in the rising process at $t = 7.0$, the velocity in the z-direction increases around the submarine. Figure 16 shows top views of the free surface behind the submarine comparing the translator movement and rising motion. In the case of the rising motion, a deep drop in the free surface behind the submarine is clearly seen. Although the effect of the rotating screw itself might not great, it is obvious that the motion of the object under the water affects the movement of the free surface. Furthermore, the simulation demonstrates the possibility of conducting useful complicated computations with the free surface.

ICCS Camera Ready Version 2021
To cite this paper please use the final published version:
DOI: 10.1007/978-3-030-77980-1_21

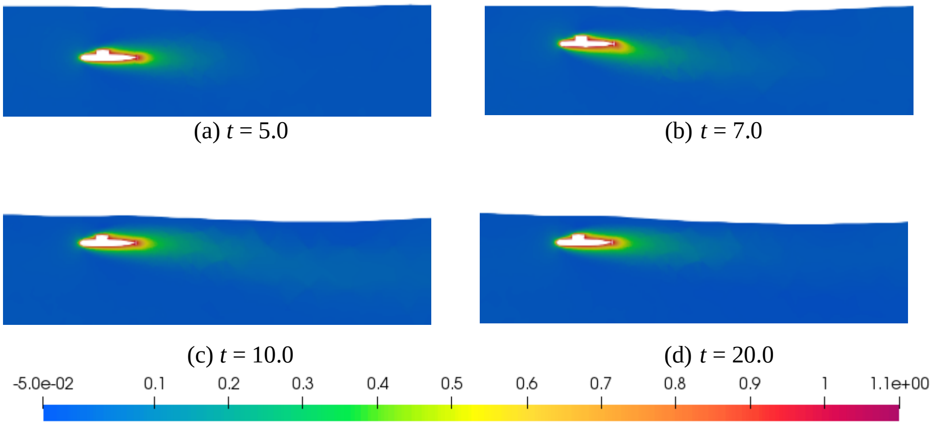

Fig. 14 x-direction velocity contours.

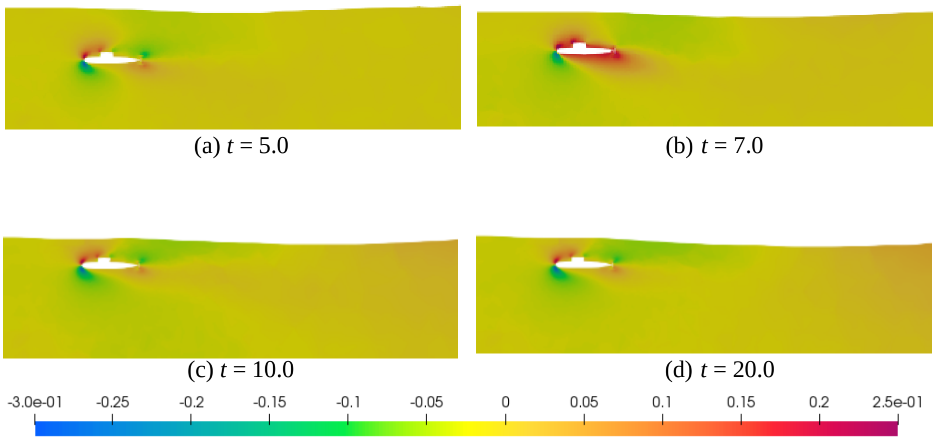

Fig. 15 z-direction velocity contours.

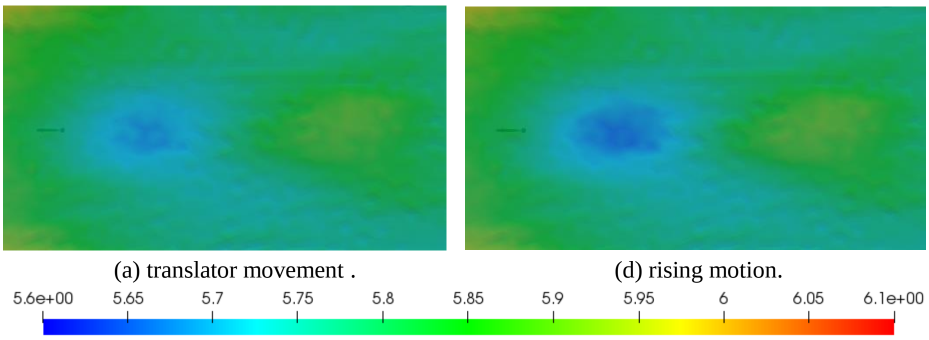

Fig. 16 Top view of free surface behind the submarine.

ICCS Camera Ready Version 2021
To cite this paper please use the final published version:
DOI: 10.1007/978-3-030-77980-1_21

4 Conclusions

Flows around a submarine with a rotating screw under the water were computed. The flows included the free water surface. To solve such a complicated combination of flows, the unstructured moving grid finite volume method and the surface height function method were used. This combined computational method could capture the uniform flow on the rotating cylindrical sliding mesh. In this test, the geometric conservation law was satisfied. The method was then applied to free surface flows around a submarine with a rotating screw. The results demonstrated the potential of a valid computation for a complicated flow field.

Acknowledgments

This publication was subsidized by the Takahashi Industrial and Economic Research Foundation.

References

1. Drew, B., et. al., A review of wave energy converter technology, Proceedings of the Institution of Mechanical Engineers, Part A: Journal of Power and Energy, Vol. 223, No. 8, pp. 887–902, (2009).
2. Mansoorzadeh, S. and Javanmard, E., An investigation of free surface effects on drag and lift coefficients of an autonomous underwater vehicle (AUV) using computational and experimental fluid dynamics methods, Journal of Fluids and Structures, Vol. 51, pp. 161–171, (2014).
3. Dean, R. G. and Dalrymple, R. A., Water Wave Mechanics for Engineers and Scientists, Advanced Series on Ocean Engineering, Vol. 2, pp. 212–260, (1991).
4. Benusiglio, A., et al., Wave drag on a submerged sphere, *Physics of Fluids*, Vol. 27, No. 072101, pp. 1–11, (2015).
5. Kwag, S., et al., Numerical Computation of 3-D Free Surface Flows by N-S Solver and Detection of Sub-breaking, *Journal of the Society of Naval Architects of Japan*, Vol. 1989, No. 166, pp. 9–16, (1989).
6. Moonesun, M., et al., Technical Notes on the Near Surface Experiments of Submerged Submarine, *International Journal of Maritime Technology*, Vol. 5, pp. 41–54, (2016).
7. C.W. Hirt and B.D. Nichols, Volume of Fluid (VOF) Method for the dynamics of Free Boundaries, *Journal of Computational Physics*, 39, pp. 201–225, (1981).
8. Yamakawa, M., et al., Numerical Simulation for a Flow around Body Ejection using an Axisymmetric Unstructured Moving Grid Method, *Computational Thermal Sciences*, Vol.4, No.3, pp. 217-223, (2012).
9. Yamakawa, M., et al., Optimization of knee joint maximum angle on dolphin kick, *Physics of Fluids* 32, 067105 (2020)
10. Yoon, S., et al., Lower-Upper Symmetric-Gauss-Seidel Method for the Euler and Navier-Stokes Equation, *AIAA Journal*, 26-9, pp. 1025-1026, (1998).
11. Vorst, H., BI-CGSTAB: a Fast and Smoothly Converging Variant of BI-CG for the Solution of Nonsymmertic Linear System, *SIAM Journal on Scientific and Statistical Computing*, 13-2, pp. 631-644, (1992).

ICCS Camera Ready Version 2021
To cite this paper please use the final published version:
DOI: 10.1007/978-3-030-77980-1_21

12. Takii, A., et al., Six degrees of freedom flight simulation of tilt-rotor aircraft with nacelle conversion, *Journal of Computational Science* 44, 101164, (2020).
13. Ito, Y., Challenges in Unstructured Mesh Generation for Practical and Efficient Computational Fluid Dynamics Simulations, *Computers and Fluids*, 85, 47-52(2013).

DOI: 10.1007/978-3-030-77980-1_21